First-Principles Study of the Structural, Electronic, and Optical Properties of Oxide-Sheathed Silicon Nanowires

Robert J. Bondi, Sangheon Lee, and Gyeong S. Hwang*

Department of Chemical Engineering, University of Texas, Austin, Texas 78712, United States

One-dimensional (1-D) nanostructures, such as silicon nanowires (SiNWs) and carbon nanotubes, have sustained intense interest because they exhibit unique, technologically significant properties that are often substantially different from their bulk counterparts as a result of various nanoscale phenomena such as quantum confinement and enormous interfacial surface areas. In particular, recent studies of SiNWs have explored numerous effects on observable properties including orientation,[1−6] passivation,[2,7,8] diameter,[1,3,9,10] cross section (shape and aspect ratio),[1,7,11] doping,[12,13] surface-to-volume ratio,[1,11] strain,[3,4,14] and surface morphologies.[12,15] The unrealized technological potential of SiNWs is vast, especially in devices already dominated by Si materials, and includes applications such as Si process-compatible optical interconnects and waveguides in complementary metal oxide semiconductor (CMOS) integrated circuits,[16] SiNW-based solar cell arrays with enhanced broad-band optical absorption,[17,18] and efficient three-dimensional anode architectures in Li-ion battery anodes.[19]

Techniques to fabricate SiNWs include both bottom-up and top-down strategies.[20] The bottom-up approach is essentially 1-D crystal synthesis involving nucleation and subsequent epitaxial growth; the most common methods are vapor−liquid−solid (VLS) and oxide-assisted growth (OAG) mechanisms.[21] VLS-grown SiNWs typically suffer from residual metal catalyst contamination, like Au or Cu,[21,22] that degrades electronic properties. OAG SiNWs can be produced by either thermal evaporation[23−26] or laser ablation[10,25] of SiO_x in a growth mechanism involving phase separation into a recrystallizing Si (c-Si) core and amorphous silicon oxide (a-SiO_x, $0 \leq x \leq 2$) sheath that is proposed[10,25] to inhibit lateral growth. The preferred orientations of OAG SiNWs are

ABSTRACT Using a density functional theory approach, we examine the dielectric function ($\varepsilon(\omega)$) optical spectra and electronic structure of various silicon nanowire (SiNW) orientations ($\langle 100 \rangle$, $\langle 110 \rangle$, $\langle 111 \rangle$, and $\langle 112 \rangle$) with amorphous oxide sheaths ($-a$-SiO_x) and compare the results against H-terminated reference SiNWs. We extend the same methods to investigate the effects of surface passivation on $\langle 111 \rangle$ SiNW properties using functional group termination ($-H$, $-OH$, and $-F$) and three different thicknesses of oxide sheath passivation. Oxide layer growth is evidenced in the spectra by concomitant appearance of tail oxide character with signatures of increased Si disorder. Suboxide contributions and increased Si disorder from oxidation average out the band structure dispersion observed in the reference SiNWs. Furthermore, we plot average Seraphin coefficients for $\langle 111 \rangle$ passivations that clearly distinguish functional group termination from surface oxidation and discuss the suboxide and disorder contributions on the characteristic intersection of these coefficients. The substantial difference in properties observed between $\langle 111 \rangle - OH$ and $\langle 111 \rangle - a$-SiO_x SiNWs emphasizes the importance of using realistic oxidation models to improve understanding of SiNW properties.

KEYWORDS: silicon nanowire · oxidation · disorder · first-principles · optical property · electronic structure

$\langle 110 \rangle$ and $\langle 112 \rangle$, where smaller diameters favor $\langle 112 \rangle$.[12,24] The top-down approach is a subtractive process that relies on combinations of high-resolution microfabrication processes, such as photolithography and etching, to delineate Si nanoscale columns on a bulk Si substrate.

While the desirable electronic properties of a-SiO_2 are arguably the primary reason for the immense proliferation of Si-based devices, accurate atomistic modeling of a-SiO_x materials and their interfaces is surprisingly limited. Tu and Tersoff[27] investigated improved models of the c-Si/a-SiO_2 interface using continuous random network model-based Metropolis Monte Carlo (CRN-MMC) simulations[28] that apply the bond switching moves of Wooten $et\ al.$[29] within the context of a Keating-like model[30] of force field energetics. Our recent effort (unpublished data) extends the work of Tu and Tersoff[27] through parametrization of a Keating-like potential optimized with the aid

of density functional theory (DFT) calculations. We further extended this structural model to the Si(001)/a-SiO$_2$ interface and revealed the sensitivity of the interface structure to the relative rigidity of the parametrized potentials in each phase (unpublished data).

Despite this recent progress on the planar Si(001)/a-SiO$_2$ interface, nanostructure oxidation can be more complex, especially in generation of physically realistic structural models. Recent first-principles studies examining structural parameters,[31] optical spectra,[32] and conductance[33] in oxidized SiNWs have provided reasonable consistency with experiment, but these SiNW oxidation models are limited to specific O influences from either hydroxyls (−OH) or bridge-bonded/back-bonded O atoms on/near the NW surface. As evidenced by experimental studies of oxidation on SiNWs[34] and Si nanocrystals (SiNCs),[35] nanoscale oxidation is more strongly influenced by certain structural parameters, including curvature and strain, than a macroscopic substrate surface, so accurate atomistic models are critical to improved understanding of nanostructure properties.

In this article, we use DFT calculations to investigate the dielectric function optical spectra and electronic structure of various SiNW orientations (⟨100⟩, ⟨110⟩, ⟨111⟩, and ⟨112⟩) with −a-SiO$_x$ surface passivations and compare the results to H-terminated reference SiNWs. In addition, we extend our computational approach to specifically examine both the chemical effects and disorder imposed by the passivation layer on ⟨111⟩ SiNWs using various functional groups (−H, −OH, and −F) and three different thicknesses of oxide sheath passivation. We also compute average Seraphin coefficients for each ⟨111⟩ SiNW passivation to identify optical signatures for both functional group surface termination and surface oxidation.

RESULTS AND DISCUSSION

Guided by the results of previous theoretical studies[1,2,5,6] and reports of commonly synthesized SiNWs,[10,24,25] we focused our investigation on four SiNW orientations: ⟨100⟩, ⟨110⟩, ⟨111⟩, and ⟨112⟩. Since as-grown SiNWs are often sheathed in passivating oxide layers, either from evolution of a native oxide,[36] intentional growth *via* subsequent thermal oxidation,[34] or remnant from NW synthesis (OAG),[10,23,25,26] we were motivated to apply our a-SiO$_x$ structural modeling procedure (unpublished data) with DFT-parametrized potential to commonly studied SiNWs to determine the influence of oxidation on observable properties.

Reference SiNWs were first constructed by extracting sections of bulk c-Si with a DFT-optimized lattice constant of 5.460 Å followed by manual termination of surface dangling bonds with various functional groups (−H, −OH, and −F). Next, these configurations were DFT-relaxed with ultrasoft pseudopotentials (US-PPs) using planewave basis sets and Γ-point Brillouin zone

TABLE 1. Structural Summary of SiNW Models[a]

SiNW	N	N_{Si}	N_O	N_H/N_F	Z_n	a_z (Å)	X,Y period (Å)	min vacuum (Å)
⟨100⟩−H	532	356		176	4	5.452	32	10.19
⟨110⟩−H	432	320		112	4	3.868	36	10.41
⟨112⟩−H	552	420		132	2	6.680	10	10.56
⟨111⟩−H	472	340		132	2	9.437	33	10.72
⟨111⟩−OH	580	340	108[b]	132	2	9.431	33	9.32
⟨111⟩−F	472	340		132	2	9.445	31	8.81
⟨100⟩−a-SiO$_x$	652	356	296		4	5.256	15	10.92
⟨110⟩−a-SiO$_x$	664	320	344		4	3.869	40	10.46
⟨112⟩−a-SiO$_x$	800	420	330		2	6.579	42	8.44
⟨111⟩−a-SiO$_x$	622	340	282		2	9.105	35	9.24
⟨111⟩−a-SiO$_x$	694	340	354		2	9.547	35	8.89
⟨111⟩−a-SiO$_x$	766	340	426		2	9.509	37	10.70

[a] X,Y supercell dimensions were individually adjusted to ensure a minimum vacuum separation >8 Å for all structures. [b] To avoid steric hindrance between some −OH groups, 24 surface sites remained −H-passivated.

(BZ) sampling (see Computational Methods). In addition, each reference SiNW was then subjected to a volume relaxation procedure that effectively optimized the period along the wire axis (a_z). Table 1 provides key structural information about each SiNW including total number of atoms (N), atomic composition (N_{Si}, N_O, N_H, and N_F), transverse period defining both X and Y supercell dimensions, and minimum vacuum spacing. Figures 1a−d and 2a,b illustrate all reference SiNW cross sections generated with this procedure while also introducing a SiNW nomenclature used throughout this article of *<hkl>*-X, where *<hkl>* designates the wire orientation and -X represents the nanowire sheath composition. Figure 2 introduces a variety of surface passivations on ⟨111⟩ SiNWs for later discussion of passivation effects.

Four independent oxidized SiNWs for each orientation and/or oxide thickness of interest were generated from the same c-Si cores as previously described. Instead of Si dangling bond surface termination with functional groups, −a-SiO$_x$ layers were generated on lateral surface facets by strategically inserting O atoms between surface Si−Si bonds. Then, amorphization of the oxide sheath layers was implemented using a procedure based on CRN-MMC simulations using our a-SiO$_x$ potential (unpublished data). Our a-SiO$_x$ potential is based on *ab initio* parametrization of a valence force field model that improves structural description of partial phase separation and mechanical properties that are experimentally observed near strained c-Si/a-SiO$_2$ interfaces. We determined the size (N) of each oxidized SiNW (−a-SiO$_x$) studied as a balance between sufficient supercell size and adequate wire length (=$Z_n \times a_z$, where Z_n is number of periods along the Z axis) to allow generation of a reasonably random amorphous layer while still being sufficiently small to practically facilitate DFT simulation. In addition, we also intended to preserve some crystallinity in the SiNW cores, so this objective limited the oxide thicknesses that could
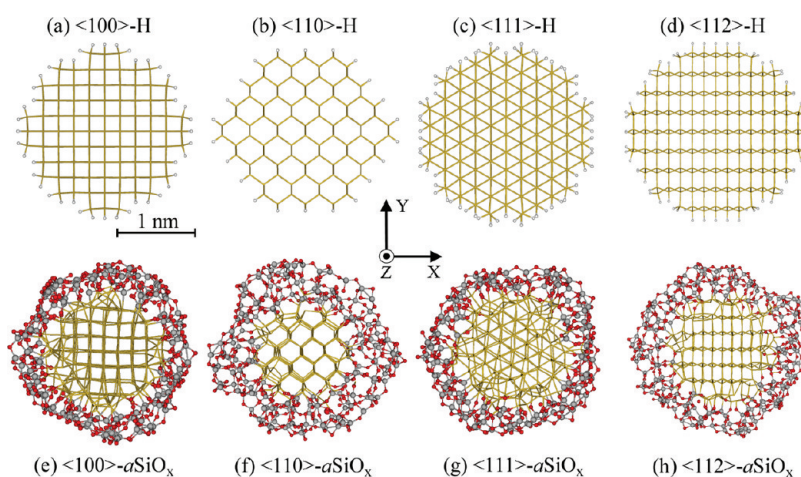
Figure 1. DFT-relaxed configuration cross sections for each SiNW orientation in both H-passivated (a−d) and corresponding oxidized (e−h) states. In all cases, the wire axis is aligned in the Z direction. Small white spheres represent H atoms. Gold wireframe depicts all Si atoms in (a−d), while in (e−h) wireframe represents only c-Si core atoms in neutral, +1, or +2 oxidation states. In the −a-SiO$_x$ sheaths, gray spheres represent Si atoms in +3 and +4 oxidation states, while medium red spheres represent O atoms. The measurement bar is scaled specifically for (a), but still provides approximate perspective for all structures shown.
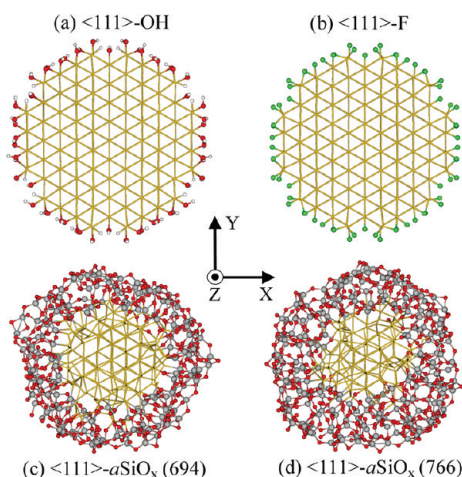

Figure 2. DFT-relaxed configuration cross sections for additional surface passivations on ⟨111⟩ SiNWs as viewed along the Z axis. Small white spheres represent H, medium red spheres represent O, and green spheres represent F. Gold wireframe depicts all Si atoms in (a,b), while in (c,d) wireframe represents only c-Si core atoms in neutral, +1, or +2 oxidation states. In the −a-SiO$_x$ sheaths, gray spheres represent Si atoms in +3 and +4 oxidation states. To prevent steric hindrance between −OH groups at 24 surface sites between the six main {110} lateral facets in (a), these sites remained −H-passivated, rather than −OH-passivated.

TABLE 2. Oxidized SiNW Suboxide Distributions

			Si oxidation state				
wire orientation	N	N$_{Si}$	0	+1	+2	+3	+4
⟨100⟩	652	356	0.46	0.10	0.05	0.11	0.29
⟨110⟩	664	320	0.37	0.05	0.04	0.13	0.41
⟨112⟩	800	420	0.45	0.06	0.06	0.10	0.34
⟨111⟩	622	340	0.47	0.08	0.06	0.10	0.29
⟨111⟩	694	340	0.37	0.07	0.04	0.14	0.38
⟨111⟩	766	340	0.29	0.04	0.05	0.15	0.48

be accommodated. Liu et al.[34] reported self-limiting oxidation in fabricated sub-5 nm SiNWs, so complete surface-initiated oxidation is indeed impractical. As shown in Figure 1, all SiNWs generated have diameters of approximately 2−3 nm.

Following simulated amorphizations to generate the −a-SiO$_x$ sheath layers, these intermediate configurations were also DFT-relaxed with US-PPs and Γ-point BZ sampling. From evaluation of the resultant DFT total energies, we selected the lowest energy structure from each four-sample set as the representative structure for

subsequent property calculations. These representative oxidized SiNWs are illustrated in Figures 1e−h and 2c,d. Table 2 provides a brief summary of the suboxide distribution for each oxidized SiNW. The minimum measured vacuum separation for any SiNW in this study is 8.44 Å (⟨112⟩−a-SiO$_x$). Our preliminary calculations showed that SiNW total energies were well-converged when vacuum separation was ≥3 Å. Unlike the reference SiNWs, we found that structure-specific volume relaxation was not effective in lowering the energy of oxidized SiNWs, so this step was omitted in the generation of optimized structural configurations for property calculations. Surrounded by an annular, interconnected −a-SiO$_x$ sheath, the dimensions of the crystalline SiNW core are highly constrained relative to its reference SiNW counterpart in which surface passivation with terminal (no interconnections) functional groups should be more flexible. This result is not surprising in the context of our parallel work (unpublished data) which shows that the oxide model produced by our DFT-parametrized a-SiO$_x$ potential has a significant influence on the planar c-Si/a-SiO$_2$ interface structure that is driven by respective strain energies of the two phases and their relative rigidity.
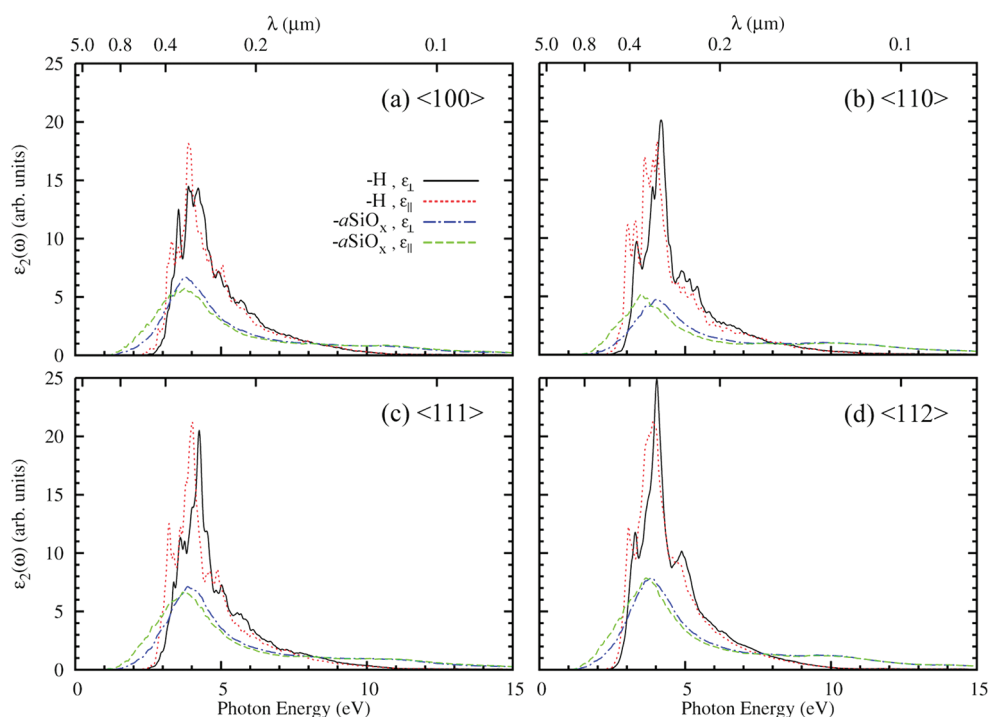
Figure 3. Imaginary components of the complex dielectric function spectra computed from DFT-GGA calculations for all SiNW configurations in Figure 1. Within each subfigure, the ε_2 components are provided both parallel ($\varepsilon_2^{\parallel}$) and perpendicular ($\varepsilon_2^{\perp}$) to each wire axis.

Optical Absorption Spectra. For all optical calculations, we utilized a four-step procedure (see Computational Methods) to compute $\varepsilon(\omega) = \varepsilon_1(\omega) + i\varepsilon_2(\omega)$ with the Vienna *ab initio* simulation package (VASP) following the general theoretical framework described by Adolph *et al.*[37] Since this calculation method is based on the independent particle approximation, quasi-particle self-energy corrections, local field effects, and excitonic contributions are neglected. The DFT approach in the generalized gradient approximation (DFT-GGA) used throughout this article characteristically underestimates the band gap (E_g), but the resulting qualitative trends are considered reliable. More discussion about this optical calculation procedure and its limitations is provided in our previous work[38,39] and in the Computational Methods section.

The study of 1-D periodic systems naturally results in the application of supercells with tetragonal symmetry where two independent components of ε_2 exist.[2] As a result, we will present both components of ε_2 for all optical spectra: (1) parallel to the wire axis, the ε_2 tensor reduces to $\varepsilon_{zz}(\omega) = \varepsilon_2^{\parallel}(\omega)$; and (2) perpendicular to the wire axis, ε_2 reduces to two identical components that will be represented as an average, $[\varepsilon_{xx}(\omega) + \varepsilon_{yy}(\omega)]/2 = \varepsilon_2^{\perp}(\omega)$.

Figure 3 introduces both $\varepsilon_2^{\parallel}(\omega)$ and $\varepsilon_2^{\perp}(\omega)$ spectral components for all four SiNW orientations representing all structures depicted in Figure 1. Similar to the results of Aradi *et al.*,[2] we observe a blue shift in the fundamental absorption edge (E_0 transition in Si) of all $\varepsilon_2^{\perp}(\omega)$ components relative to $\varepsilon_2^{\parallel}(\omega)$ for all orientations

and surface passivations ($-H$ and $-a$-SiO$_x$). Since the SiNWs we present have larger diameters than those of Aradi *et al.*, the degree of shift we observe is generally smaller because the quantum confinement (QC) effect on the $\perp$ components is diminished.

On the basis of a previous report,[40] the perceived reduction in anisotropy with reduced QC is a misleading conclusion that arises from approximations made in sampling optical transitions. Bruneval *et al.*[40] made the critical observation that the approximations in this established optical calculation method,[37] especially in neglecting local field (LF) effects, do not allow accurate description of anisotropy at this scale. Bruneval *et al.* further show that first-principles calculations including LF effects and classical estimations based on effective medium theory indicate that optical anisotropy remains even while QC effects are vanishing.

As anticipated, growth of the $-a$-SiO$_x$ surface layer on all SiNW orientations has an appreciable and consistent effect on $\varepsilon_2(\omega)$. For all cases in Figure 3, the $-a$-SiO$_x$ passivation diminishes the main absorption peak (E_2 transition in Si) near 4 eV relative to the $-H$ reference NWs and also washes out most characteristic c-Si transition edges and peaks. Since the growth of the $-a$-SiO$_x$ layer results in a two-phase nanostructure, the optical spectra consequently represent a weighted hybrid of both distorted c-Si and a-SiO$_x$ responses. The growth of the a-SiO$_x$ surface layer creates strain in the c-Si NW cores and disorder at the c-Si/a-SiO$_x$ interface that can be viewed as incipient amorphization of the c-Si core; despite this, the remnant E_2 Si
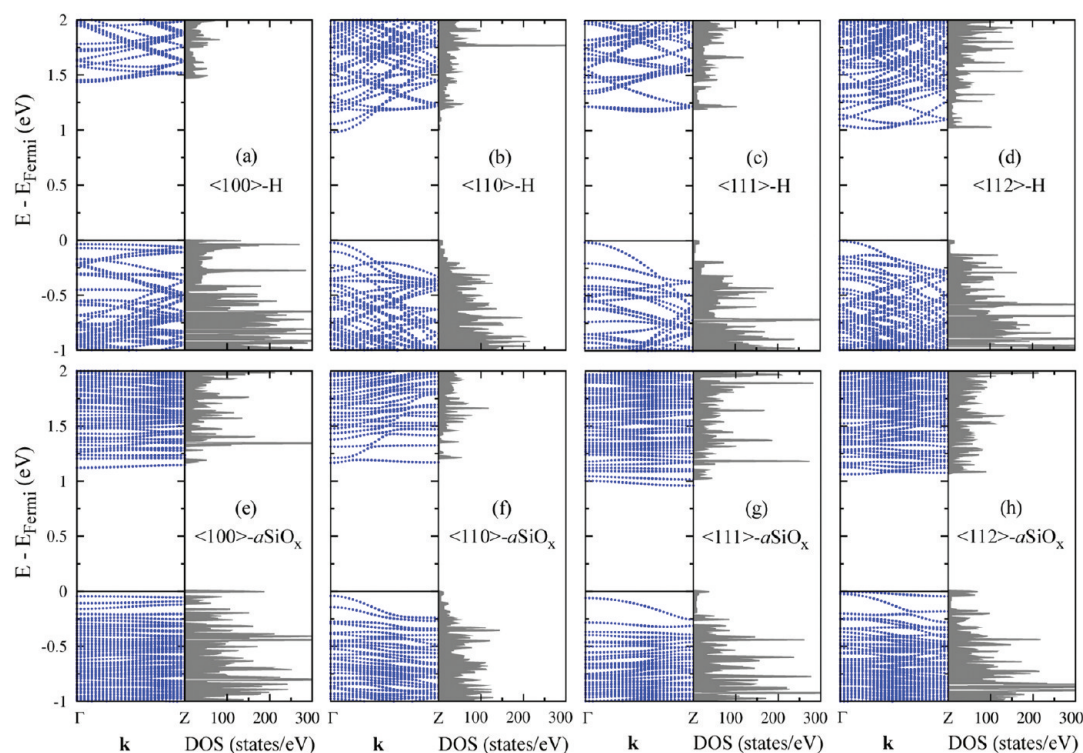
Figure 4. Band structure and total DOS computed from DFT-GGA calculations for each SiNW configuration shown in Figure 1. The top panels represent −H reference SiNWs, while the corresponding bottom panels represent the oxidized SiNW for each orientation. Reference Fermi energies for band structures are computed during determination of the charge density distribution. Some variation in energy referencing between band structure and DOS calculations is an inevitable consequence of different k-point sampling schemes.

peak remains. The other $\varepsilon_2(\omega)$ contribution from the oxide phase is represented by the long tails present for all −a-SiO$_x$ SiNW orientations that gently rise to almost imperceptible peaks near 10 eV, consistent with our previous results for SiO$_2$ optical response (see Figures 5 and 6 in ref 38). Despite significant residual crystallinity visually apparent in the core of each −a-SiO$_x$ SiNW (see Figure 1e−h), our optical spectra reinforce the acute sensitivity of optical techniques in semiconductor characterization.[15,41,42]

Electronic Structure. In Figure 4, we present the band structure and total density of states (DOS) for all nanowires represented in Figure 1. We find that the band structures exhibited by the −H SiNWs are qualitatively consistent with results in the literature; however, the relatively larger[2,5−7] −H reference SiNWs we investigate (E_g scales down with increasing diameter) and the various functionals[2,3,7] and E_g corrections[5,6] employed in other studies understandably impart some quantitative variations. We observe direct gaps for both ⟨100⟩−H and ⟨110⟩−H, while ⟨111⟩−H and ⟨112⟩−H exhibit indirect gaps. Similar to the work of Scheel et al.,[6] we also observe that the direct nature, essential for photonic applications, of ⟨110⟩−H is dampened by a low population of states near the gap which effectively nullifies the direct gap character for device operation.

The most interesting aspect of our band structure results lies in comparison of each reference SiNW

(Figure 4a−d) with its corresponding oxidized SiNW (Figure 4e−h). For all wire orientations, it is readily apparent that the usual energy dispersions with respect to **k** are averaged and flattened out with the growth of the −a-SiO$_x$ layer relative to the reference SiNWs. We attribute this result to the disorder imposed on the SiNW cores as a result of their close proximity to the c-Si/a-SiO$_x$ interface since the band structure we observe on the oxidized SiNWs is similar to what might be expected at the onset of amorphization. As the configuration approaches complete amorphization, all remnant band structure should disappear as **k** becomes undefined. For the case of ⟨100⟩−a-SiO$_x$ (Figure 4e), the band structure has almost reduced to an elaborate, but redundant, plot of band gap states as a result of the flat nature and high density of bands present. Note that this is also partially a function of the ⟨100⟩−H band structure since the energy dispersions along the bottom of the conduction band and top of the valence band are inherently subtle in this orientation. In other cases, such as the ⟨110⟩ and ⟨111⟩ SiNWs, the oxidized SiNW band structure is more easily seen as a **k**-averaged counterpart of the corresponding −H SiNW band structure.

Another interesting consequence of the evolution of SiNW disorder in the core is the effect on the direct/indirect nature of the band gap. Previous studies[3,4,14] have examined the effect of applied strain on both the

magnitude and nature of the SiNW E_g, including reports[4] that specific strain conditions can change the nature of the gap. Other studies[31,32] have also provided insight into the effect of O incorporation on QC in SiNCs. As Ramos et al. report,[32] the effect of O incorporation is complicated by competing effects. On one hand, oxidation of the surface increases the nanostructure diameter, which reduces QC and E_g; however, O incorporation via back-bond oxidation effectively reduces the c-Si core, which increases QC and E_g. The growth of amorphous oxide layers on SiNWs introduces an additional structural influence that promotes averaging of **k** in the band structure which can shift the k-point coordinate of both conduction band minima (CBM) and valence band maxima (VBM).

As a result of these competing oxidation effects, we observe different band structure changes from SiNW oxidation. In Figure 4, we observe the magnitude of E_g to shrink for ⟨100⟩- and ⟨111⟩-oriented SiNWs, while E_g increases for both the ⟨110⟩ and ⟨112⟩ cases. Analyzing Figure 4 in terms of SiNW gap character, the **k**-averaging effect of oxidation on the CBM around Γ almost destroys the strongly direct appearance of the ⟨110⟩ SiNW E_g (Figure 4b,f). However, comparison of the ⟨112⟩ SiNWs (Figure 4d,h) indicates that oxidation of the surface has changed the nature of the gap from indirect to a weakly direct character since **k**-averaging has moved the k-point coordinate of CBM to Γ.

Surface Passivation Effect on Optical Properties. To better understand the effect of various surface passivations, we chose the commonly synthesized ⟨111⟩ wire orientation for further examination. Figures 1c,g and 2 collectively illustrate three functional group (−H, −OH, and −F) passivations to assess chemical effects as well as three different thicknesses of oxide sheath passivation (622, 694, and 766 atom ⟨111⟩−a-SiO$_x$) to study the expected effects of variable oxide thickness. In particular, the functional groups provide a basis for comparison of electronegativity (EN) influence. On the Pauling scale, the EN values of the relevant elements are 1.9, 2.2, 3.4, and 4.0 for Si, H, O, and F, respectively.[43] For the −a-SiO$_x$ passivations, we expect to observe variation in interface composition (suboxide distribution) and degree of strain/disorder imparted on the c-Si core with oxide thickness. Revisiting Table 2, we see that the suboxide (Si^{1+}, Si^{2+}, Si^{3+}) fraction of Si atoms remains nearly constant at ∼0.25 for ⟨111⟩ SiNWs; however, the nature of the interface changes with increasing oxide thickness because the Si^{3+} population is increasing at the expense of the Si^{1+} population.

Figure 5 extends our results shown in Figure 3c with separate plots for $\varepsilon_2^\parallel$ and $\varepsilon_2^\perp$ that show the influence of surface passivation on the optical spectra. Using ⟨111⟩−H as the base reference, substitution of −H with either −OH or −F has a similar effect on both components of ε_2. Substitution with −F reduces and red shifts
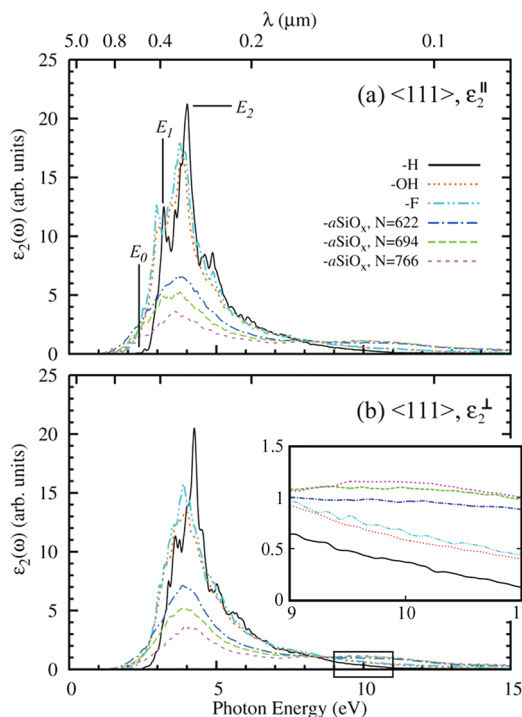

Figure 5. (a) Parallel and (b) perpendicular components of the imaginary parts of the complex dielectric function spectra computed from DFT-GGA calculations for all ⟨111⟩ SiNW passivations. The optical transitions annotated in (a) for ⟨111⟩−H follow the nomenclature of Yu and Cardona.[42] The tail spectra magnified in the inset in (b) have the same trend for (a) and are therefore omitted in (a).

the E_2 peak and also red shifts E_0; substitution with −OH further reduces the E_2 peak intensity and shows a similar red shift in both E_2 and E_0 as observed for the −F case. The E_1 peak (between E_0 and E_2) is particularly apparent in $\varepsilon_2^\parallel$ for the three cases of surface termination with functional groups. For ⟨111⟩−H, the $E_1^\parallel$ transition occurs at 3.22 eV; however, substitution with either −F or −OH red shifts the $E_1^\parallel$ peak to 2.97 and 3.03 eV, respectively. While the $E_1^\perp$ peak is evident for the −H case in $\varepsilon_2^\perp$, the $E_1^\perp$ peak is no longer apparent for −OH and −F passivations. Furthermore, substitution of −H with either −OH or −F also increases the high energy tail (>10 eV) in both $\varepsilon_2^\parallel$ and $\varepsilon_2^\perp$ spectra. Aradi et al.[2] observed similar red shifting of E_0 on both ⟨110⟩ and ⟨112⟩ SiNWs when −H passivation was substituted with −OH passivation, which they attributed to reduced band gaps from the high EN (3.4) of O in the −OH groups. Nolan et al.[8] also show band gap reduction on ⟨100⟩ SiNWs passivated with −OH groups.

For the ⟨111⟩−a-SiO$_x$ SiNWs, we observe the expected results in Figure 5 for both ε_2 components of Si E_2 peak intensity reduction and broadening in correlation with increased oxide thickness. This optical response is not only characteristic of amorphization[38,39] but also a signature of stoichiometric shift in bulk a-SiO$_x$ ($0 \le x \le 2$) as x increases.[38] If the oxide contribution in these SiNWs was increased following further
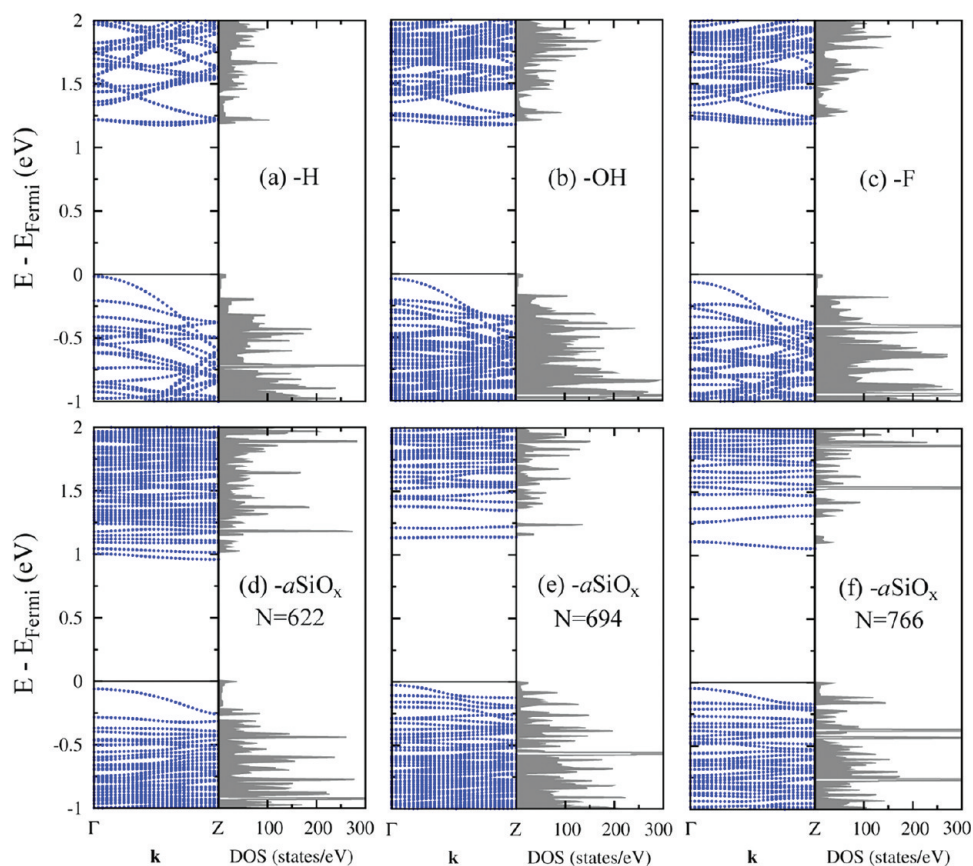
Figure 6. Band structure and total DOS computed from DFT-GGA calculations for all $\langle 111 \rangle$ SiNW passivations. The top panels represent SiNWs passivated with functional groups, while the bottom panels represent the effect of increasing oxidation from left to right. Reference Fermi energies for band structures are computed during determination of the charge density distribution. Some variation in energy referencing between band structure and DOS calculations is an inevitable consequence of different k-point sampling schemes.

oxidation, we expect that a blue shift in the E_2 peak would also become evident (see Figure 5 in ref 38). In addition, closer inspection of Figure 5b *via* the inset shows the main characteristic SiO_2 $\varepsilon_2(\omega)$ peak near 10 eV increasing as the oxide sheath thickness increases.

Surface Passivation Effect on Electronic Structure. Figure 6 extends our results in Figure 4 with a comparison of $\langle 111 \rangle$ SiNW band structures resulting from all six surface passivations. Substitution of $-H$ with $-OH$ (Figure 6b) has modest implications on the band structure; the most obvious effect is simply an increase in band density that is also reflected as a general rise in DOS. Substitution of $-OH$ with $-F$ (Figure 6c) results in few modifications in the electronic structure. In contrast, the effects of increasing oxidation on the $\langle 111 \rangle$ SiNW is more interesting (see Figures 6d$-$f). We expected the degree of disorder present for the $N = 766$ case to fully average out any remaining dispersion in the band structure, but this is not observed. Increased oxidation among the three $\langle 111 \rangle - a\text{-}SiO_x$ cases ($N = 622, 694,$ and 766 atoms) has the general effect of making the DOS increasingly sparse and more discontinuous with respect to energy. The increasingly sparse nature of near-gap states is a consequence of complete Si oxidation. While Si^0 and the suboxide states contribute to near-gap

electronic structure, the influence of Si^{4+} is farther removed (E_g for SiO_2 $\sim$9 eV (ref 44)).

Interestingly, the gap for $N = 694$ becomes weakly direct after oxidation, although the sparse DOS in the CB precludes applicability to photonic devices and nearly flat CBs correspond to large electron effective masses. Measurements on oxidized SiNWs in this size regime support reduced mobility, which is a proposed consequence of increased interfacial scattering.[45] In addition, reduced mobility is also an expected consequence of increased disorder since carrier mobilities in a-Si are typically orders of magnitude smaller than in c-Si. While we observe that oxidation is capable of changing the direct/indirect nature of the gap in Figure 6d$-$f, we can speculate that a statistical sampling of oxidized SiNWs would reveal that the random nature of $-a\text{-}SiO_x$ yields mixed distributions of direct/indirect SiNWs for each oxide thickness. We suspect that oxidation-induced disorder is responsible for changing the direct/indirect nature of the gap; however, oxidation may not be a reliable tool to augment gap character because the random aspect of **k**-averaging will likely make the direction of change hard to control.

Carrier *et al.*[44] studied Si/SiO_2 superlattice interfaces to reach the conclusion that the suboxide is

responsible for the nearly dispersionless (**k**-invariant) bands; however, since the oxide is simultaneously responsible for both suboxide influence (Si charge states) and imposition of disorder in the *c*-Si phase, the relative contribution of each effect remains to be determined. We can point out that −OH passivation (Figure 6b) produces a near-surface population of Si^{1+}, yet the band structure is hardly dispersionless.

Optical Characterization with Seraphin Coefficients. Previous reports[41,46] used Seraphin coefficients to optically characterize the structure of bulk semiconductors and heterostructures based on the original work of Seraphin and Bottka.[47] We will demonstrate the use of optical calculation techniques to help illuminate the relationship between the atomic structure of differently passivated SiNWs and the response of Seraphin coefficients with specific attention given to the contributions of the suboxide layer and structural disorder from oxide passivations.

Experimental studies based on Seraphin coefficients[47] use various modulation spectroscopies[48] to structurally characterize Si, such as determination of intrinsic interface strain[46] and disorder.[41] We similarly follow the method described by Sundari *et al.*[41] since all necessary quantities are extracted from $\varepsilon(\omega)$ for an arbitrary material, which is typically a semiconductor. The ratio of change in reflectivity (ΔR) to absolute reflectivity (R) is calculated as

$$\Delta R/R = \alpha \Delta \varepsilon_1 + \beta \Delta \varepsilon_2 \qquad (1)$$

where $\Delta \varepsilon_1$ and $\Delta \varepsilon_2$ are changes in respective components of the complex dielectric function, $\alpha = 2A/(A^2 + B^2)$, $\beta = 2B/(A^2 + B^2)$, $A = n(n^2 - 3k^2 - 1)$, and $B = k(3n^2 - k^2 - 1)$. The frequency-dependent quantities, α and β, are the Seraphin coefficients[47] and n and k are the real and imaginary parts,[49] respectively, of the complex refractive index:

$$n(\omega) = \left[\frac{\sqrt{\varepsilon_1^2(\omega) + \varepsilon_2^2(\omega)} + \varepsilon_1(\omega)}{2}\right]^{1/2} \qquad (2)$$

$$k(\omega) = \left[\frac{\sqrt{\varepsilon_1^2(\omega) + \varepsilon_2^2(\omega)} - \varepsilon_1(\omega)}{2}\right]^{1/2} \qquad (3)$$

The work of Sundari *et al.* shows that determining the frequency or energy ($E = \hbar\omega$) of intersection between α and β, which they denote as the crossover energy (E_c), can be used as a reliable method to quantify bulk Si structural disorder.

In Figure 7, we plot α and β derived from both ∥ and ⊥ components of calculated $\varepsilon(\omega)$ for the various investigated surface passivations of ⟨111⟩ SiNWs. We also provide Figure 8 as a reference to illustrate the behavior of α and β strictly for changes in phase and composition for the relevant bulk structures of *c*-Si, *c*-SiO₂, and *a*-SiO$_x$ (x = 0, 0.5, 1.0, 1.5, and 2.0). In Figure 7, the qualitative result is the same for both components,
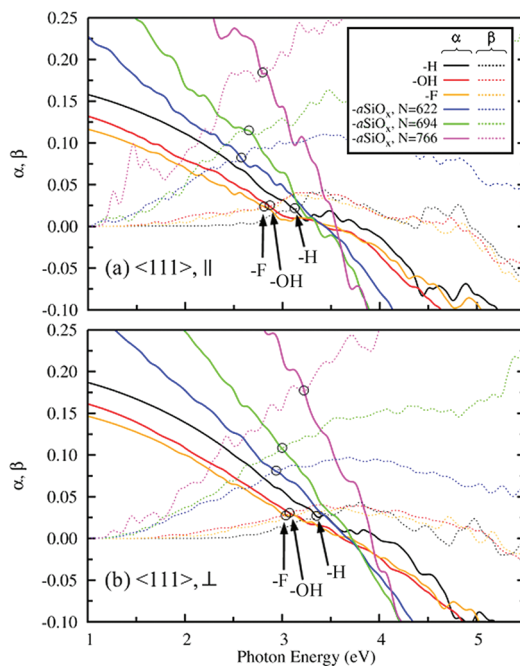

Figure 7. Seraphin coefficients evaluated from (a) parallel and (b) perpendicular components of the dielectric function spectra computed from DFT-GGA calculations for all ⟨111⟩ SiNW passivations. Solid lines represent α values, and dashed lines represent β values. The crossover energies (E_c) for each SiNW are identified by open circles for clarity.

although the ⊥ components are again blue-shifted relative to the ∥ components. We demarcate the α/β intersections (E_c) with circles for each SiNW. When −H is substituted with higher EN functional groups, we observe E_c to red shift from 3.12 eV (Figure 7a). In contrast, the ⟨111⟩−*a*-SiO$_x$ SiNWs exhibit a different trend. E_c for the 622 atom SiNW occurs near 2.5 eV (Figure 7a); increased oxidation of the SiNW largely results in the vertical coordinate of E_c increasing with a slight blue shift. Note that α and β are representative of the comprehensive oxidized SiNW structure (*c*-Si and *a*-SiO$_x$ phases). Giri *et al.*[50] mention the significance of explicitly accounting for each phase *via* multilayer model fitting in spectroscopic ellipsometry; however, since we do not attempt to extract numerical parameters from our analysis, we believe that our demonstration of qualitative discernment among various surface passivations using Seraphin coefficients is a meritable contribution.

Inspection of Figure 8 illustrates three significant details about the behavior of Seraphin coefficients in SiO$_x$ structures. First, amorphization of Si appears strictly as a red shift in E_c as emphasized by Sundari *et al.*[41] Second, increasing oxide character (x) in *a*-SiO$_x$ has a substantial influence on both vertical and horizontal coordinates of E_c. Third, the effect of *c*-SiO₂ amorphization is largely observed as change in vertical coordinate of E_c. In comparison, the oxide composition contribution appears to be a stronger influence on α and β than the induced structural disorder. In the
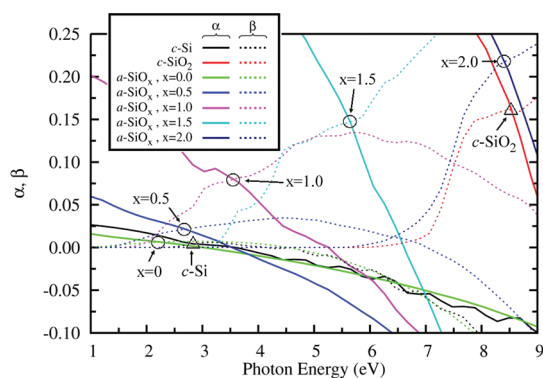
Figure 8. Seraphin coefficients evaluated from DFT-GGA calculations for bulk c-Si, c-SiO$_2$ (α-quartz), and a-SiO$_x$ ($x = 0$, 0.5, 1.0, 1.5, and 2.0) reference structures. All structures and their $\varepsilon_2(\omega)$ were previously described in ref 38. Solid lines represent α values, and dashed lines represent β values. Crossover energies (E_c) are identified by open circles for a-SiO$_x$ structures and open triangles for the limiting crystalline cases.

TABLE 3. ⟨111⟩ SiNW Bond Topology Statistics

passivation	N	bond length^a Si—Si (Å)	bond angle^b Si—Si—Si (deg)	Si—O—Si (deg)
—a-SiO$_x$	622	2.362 ± 0.050	109.0 ± 9.2	131.9 ± 17.7
—a-SiO$_x$	694	2.390 ± 0.056	109.1 ± 9.2	133.7 ± 18.7
—a-SiO$_x$	766	2.382 ± 0.057	109.0 ± 9.9	134.4 ± 18.1
—H	472	2.363 ± 0.003	109.5 ± 0.9	

^{a} —a-SiO$_x$ wires represent only Si^0 state atoms. —H reference excludes perimeter Si atoms with H neighbors. All values are given as mean $\pm$ standard deviation. ^{b} Values represent all bond angles in each SiNW.

context of oxidized SiNWs, we can interpret the Seraphin coefficient behavior (Figure 7) with the following contributions: (1) the blue shift and increasing E_c vertical coordinate with increasing oxidation is largely driven by changes in constituent Si oxidation states; (2) the energy coordinates for all three E_c values are somewhat red-shifted relative to the —H case as a result of disorder; and (3) increasing Si disorder with increasing oxidation might be manifested as an increase in slope of the E_c trend.

Oxidation Effect on Structure. The —a-SiO$_x$ SiNW cross sections (see Figures 1g and 2c,d) illustrate a qualitative increase in disorder as oxide thickness increases. We provide a brief summary in Table 3 of the structural changes incurred from oxidation of the ⟨110⟩ lateral facets of ⟨111⟩-oriented SiNWs. We expected to observe an increasing compressive character of the core Si—Si bonds, but that trend is not readily apparent in Table 3. Instead, the 622 atom —a-SiO$_x$ wire has an average bond length (2.362 Å) nearly identical to the —H reference SiNW (2.363 Å). Further oxidation ($N = 694$ and 766 cases) actually increases the average Si—Si bond length. The average Si—Si—Si bond angle from the —H reference case (109.5 $\pm$ 0.9°) is decreased following oxidation, and the introduced disorder is evidenced by an order of magnitude increase in the standard deviation. A trend for increased Si—O—Si bond angle approaching that of bulk a-SiO$_2$ (151 $\pm$ 11° Å)[51] is observed as the oxidation thickness is increased on ⟨111⟩—a-SiO$_x$ SiNWs. Note that one limitation of Monte Carlo methods in oxidation simulations is the inability to capture kinetically limited processes during structural relaxation; as a consequence, some resultant structures can be over-relaxed and thus distort some structural statistics.

As other reports indicate,[31,35] the structural effects of oxidation on Si nanostructures is a complex, multivariate problem. Hofmeister et al.[35] synthesized

oxidized SiNCs from silane pyrolysis and demonstrated that SiNCs with diameters <3 nm (c-Si core) exhibit core tension, while SiNCs of larger diameter exhibit core compression relative to bulk Si. They attribute the observed diameter-dependent sign of core strain to an estimated negative interfacial stress contribution. Our SiNW results are qualitatively similar to the SiNC results of Hofmeister et al. We have presented oxidized ⟨111⟩ SiNWs with core diameters <3 nm that exhibit core tension; on the other hand, we have also generated larger oxidized SiNWs (diameter ~ 10 nm, $N \sim 10^4$ atoms) in our unpublished work that indeed exhibit compressive strain in the Si core (magnitude dependent on oxide thickness) relative to the bulk Si—Si bond length (2.363 Å).

SUMMARY

In summary, we applied a custom CRN-MMC simulation procedure to generate amorphous oxide layers on four important orientations of SiNWs (⟨100⟩, ⟨110⟩, ⟨111⟩, and ⟨112⟩) to study the effects of wire orientation, surface passivation, and degree of strain/disorder in the c-Si core on resultant optical spectra and electronic structure. To isolate the effects of surface passivation, we examined the ⟨111⟩ SiNW orientation passivated with three different functional groups (—H, —F, and —OH) and three thicknesses of oxide sheath (622, 694, and 766 atom ⟨111⟩—a-SiO$_x$). The surface passivation effects discussed will likely exhibit similarities on other SiNW orientations, but we do not infer transferability of these trends without further analysis.

For all SiNW orientations, the effect of oxidation on both $\varepsilon_2^{\parallel}(\omega)$ and $\varepsilon_2^{\perp}(\omega)$ dielectric function spectra shows consistent and appreciable reduction in the Si E_2 transition peak, red shift in fundamental absorption edge (E_0), and appearance of a high energy tail peaking near 10 eV representing the oxide contribution. The effect of quantum confinement imparts a blue shift on all $\varepsilon_2^{\perp}$ components relative to $\varepsilon_2^{\parallel}$. Our band structure calculations indicate an onset of amorphization resulting from oxidation as the disintegration of crystalline order is evidenced by smoothing of all bands in the gap vicinity that is attributed to k-point averaging along the

SiNW axis. For the $\langle 112 \rangle - a\text{-}SiO_x$ SiNW, k-point averaging changes the nature of the band gap from indirect to direct by moving the conduction band minimum to Γ.

The effect of surface passivation on the $\langle 111 \rangle$ SiNW in the $\varepsilon_2^{\parallel}$ spectra by substitution of $-H$ with either $-F$ or $-OH$ groups is similar: (1) red shift and reduction of $E_2^{\parallel}$ peak, (2) red shift in both $E_1^{\parallel}$ and $E_0^{\parallel}$ transitions, and (3) increase in high energy tail intensity. Similar effects are seen for $\varepsilon_2^{\perp}$, but the $E_1^{\perp}$ peak is no longer evident with electronegative $-F$ or $-OH$ passivations. Influenced by previous employment of Seraphin coefficients (α and β) to optically characterize semiconductor structures, we computed average α and β from spectra for all six $\langle 111 \rangle$ SiNW surface passivations to evaluate the optical contributions of suboxide composition and disorder. Our results show a unique crossover energy (E_c) for each case and a clear distinction between functional group passivations and oxidation layers. In addition, increasing oxide thickness is identified using Seraphin coefficients as an increase mostly in the vertical coordinate of E_c, which was shown to correlate largely to increasing oxide character (x) in $a\text{-}SiO_x$. Our electronic and optical characterization of SiNWs passivated with amorphous oxide layers extends current understanding of these technologically interesting nanostructures, particularly in revealing how oxidation-induced disorder and composition modulate predicted properties.

TABLE 4. Essential DFT Conditions

SiNW	E_{cut} (eV)[a]	tolerance ($\times 10^{-2}$ eV/Å)[b]	conduction bands[c]
$\langle 100 \rangle - H$	160(250)	5	900(300)
$\langle 110 \rangle - H$	160(250)	5	900(300)
$\langle 112 \rangle - H$	160(250)	5	900(300)
$\langle 111 \rangle - H$	160(250)	5	900(300)
$\langle 111 \rangle - OH$	270(300)	7.5	1200(400)
$\langle 111 \rangle - F$	273(250)	5	1200(400)
$\langle 100 \rangle - a\text{-}SiO_x$	270(300)	7.5	1200(400)
$\langle 110 \rangle - a\text{-}SiO_x$	270(300)	7.5	1200(400)
$\langle 112 \rangle - a\text{-}SiO_x$	270(300)	7.5	1200(400)
$\langle 111 \rangle - a\text{-}SiO_x$	270(300)	7.5	1200(400)
$\langle 111 \rangle - a\text{-}SiO_x$	270(300)	7.5	1200(400)
$\langle 111 \rangle - a\text{-}SiO_x$	270(300)	7.5	1200(400)

[a] Values are first provided for structural optimization and in () when optimized ionic coordinates were fixed for optical and electronic calculations. [b] Force-based ionic convergence criteria. [c] Values are first given for optical calculations and in () for electronic structure calculations.

COMPUTATIONAL METHODS

Density Functional Theory. The nanowire configurations, optical spectra, and electronic structure calculations presented were all computed using a planewave pseudopotential approach within the generalized gradient approximation of Perdew and Wang (GGA-PW91)[52] to DFT,[53] as implemented in VASP.[54] We used Vanderbilt-type US-PPs[55] to represent the interaction between ion cores and valence electrons for initial structural optimization and during volume relaxation of functionally passivated ($-H$, $-OH$, and $-F$) SiNWs; projector-augmented wave (PAW) pseudopotentials[56] were employed for all optical and electronic calculations. The PAW methodology effectively comprises an all-electron frozen-core representation that describes exact valence wave functions; therefore, we employed PAW pseudopotentials to help ensure enhanced representations of electronic transitions. Table 4 summarizes all kinetic energy cut-offs (E_{cut}), force-based ionic convergence criteria, and conduction bands simulated for each SiNW presented.

Optical Calculation Procedure. A four-step procedure was employed in all optical calculations to calculate $\varepsilon(\omega)$. In the first step, the ionic configuration of each SiNW was optimized with PAW pseudopotentials and Γ-point BZ sampling using the conditions shown in Table 4. Second, the charge density distribution was determined with the BZ sampling increased to a $1 \times 1 \times 10$ Γ-centered mesh,[54] which results in six k-points in the irreducible BZ along the axis for all SiNWs. Third, the frequency-dependent dielectric matrix was determined from the optimized charge density distribution with the tetrahedron method[54] and an adequate number of conduction bands (see Table 4) that we adjusted according to surface passivation. Fourth, the OPTICS code of Fürthmuller[57] was employed to obtain both the imaginary part (ε_2) of $\varepsilon(\omega)$ by sampling optical transitions up to 20 eV and compute the real part (ε_1) through application of the Kramers−Kronig transformation.

Electronic Structure Calculations. For computation of band structure and DOS, we started from the charge density distributions previously determined during calculation of $\varepsilon(\omega)$. For each SiNW, we evaluated the energy dispersion relationship along the wire axis using 30 k-points along a line from Γ to Z, where Z is Π/a_z along an arbitrary wire axis to the BZ edge. Since we only present electronic structure in the proximity of the band gap, we reduced the number of conduction bands included for both band structure and DOS calculations to 1/3 of the value used for optical calculations as summarized in Table 4. For DOS calculations, we reverted to the same $1 \times 1 \times 10$ k-point mesh employed for optical calculations.

REFERENCES AND NOTES

1. Zhang, R. Q.; Lifshitz, Y.; Ma, D. D. D.; Zhao, Y. L.; Frauenheim, Th.; Lee, S. T.; Tong, S. Y. Structures and Energetics of Hydrogen-Terminated Silicon Nanowire Surfaces. *J. Chem. Phys.* **2005,** *123*, 144703.

2. Aradi, B.; Ramos, L. E.; Deák, P.; Köhler, Th.; Bechstedt, F.; Zhang, R. Q.; Frauenheim, Th. Theoretical Study of the Chemical Gap Tuning in Silicon Nanowires. *Phys. Rev. B* **2007,** *76*, 035305.

3. Leu, P. W.; Svizhenko, A.; Cho, K. *Ab Initio* Calculations of the Mechanical and Electronic Properties of Strained Si Nanowires. *Phys. Rev. B* **2008,** *77*, 235305.

4. Hong, K.-H.; Kim, J.; Lee, S.-H.; Shin, J. K. Strain-Driven Electronic Band Structure Modulation of Si Nanowires. *Nano Lett.* **2008,** *8*, 1335–1340.

5. Li, J.; Freeman, A. J. First-Principles Determination of the Electronic Structures and Optical Properties of One-Nanometer (001) and (111) Si Nanowires. *Phys. Rev. B* **2006,** *74*, 075333.

6. Scheel, H.; Reich, S.; Thomsen, C. Electronic Band Structure of High-Index Silicon Nanowires. *Phys. Status Solidi B* **2005,** *242*, 2474–2479.

7. Hmiel, A.; Xue, Y. Shape-Tunable Electronic Properties of Monohydride and Trihydride [112]-Oriented Si Nanowires. *Phys. Rev. B* **2009,** *80*, 241410(R).

8. Nolan, M.; O'Callaghan, S.; Fagas, G.; Greer, J. C. Silicon Nanowire Band Gap Modification. *Nano Lett.* **2007,** *7*, 34–38.

9. Bhattacharya, S.; Banerjee, D.; Adu, K. W.; Samui, S.; Bhattacharyya, So. Confinement in Silicon Nanowires: Optical Properties. *Appl. Phys. Lett.* **2004,** *85,* 2008–2010.

10. Zhang, Y. F.; Tang, Y. H.; Wang, N.; Lee, C. S.; Bello, I.; Lee, S. T. One-Dimensional Growth Mechanism of Crystalline Silicon Nanowires. *J. Cryst. Growth* **1999,** *197,* 136–140.

11. Yao, D.; Zhang, G.; Li, B. A Universal Expression of Band Gap for Silicon Nanowires of Different Cross-Section Geometries. *Nano Lett.* **2008,** *8,* 4557–4561.

12. Singh, A. K.; Kumar, V.; Note, R.; Kawazoe, Y. Effects of Morphology and Doping on the Electronic and Structural Properties of Hydrogenated Silicon Nanowires. *Nano Lett.* **2006,** *6,* 920–925.

13. Moon, C.-Y.; Lee, W.-J.; Chang, K. J. Formation of Dopant-Pair Defects and Doping Efficiency in B- and P-Doped Silicon Nanowires. *Nano Lett.* **2008,** *8,* 3086–3091.

14. Maegawa, T.; Yamauchi, T.; Hara, T.; Tsuchiya, H.; Ogawa, M. Strain Effects on Electronic Bandstructures in Nanoscaled Silicon: From Bulk to Nanowire. *IEEE Trans. Electron Devices* **2009,** *56,* 553–559.

15. Zhang, Y. F.; Liao, L. S.; Chan, W. H.; Lee, S. T.; Sammynaiken, R.; Sham, T. K. Electronic Structure of Silicon Nanowires: A Photoemission and X-ray Absorption Study. *Phys. Rev. B* **2000,** *61,* 8298–8305.

16. Dai, D.; Shi, Y.; He, S. Comparative Study of the Integration Density for Passive Linear Planar Light-Wave Circuits Based on Three Different Kinds of Nanophotonic Waveguide. *Appl. Opt.* **2007,** *46,* 1126–1131.

17. Stelzner, Th.; Pietsch, M.; Andrä, G.; Falk, F.; Ose, E.; Christiansen, S. Silicon Nanowire-Based Solar Cells. *Nanotechnology* **2008,** *19,* 295203.

18. Garnett, E. C.; Yang, P. Silicon Nanowire Radial p−n Junction Solar Cells. *J. Am. Chem. Soc.* **2008,** *130,* 9224–9225.

19. Kang, K.; Lee, H.-S.; Han, D.-W.; Kim, G.-S.; Lee, D.; Lee, G.; Kang, Y.-M.; Jo, M.-H. Maximum Li Storage in Si Nanowires for the High Capacity Three-Dimensional Li-ion Battery. *Appl. Phys. Lett.* **2010,** *96,* 053110.

20. Chen, S.; Bomer, J. G.; van der Wiel, W. G.; Carlen, E. T.; van den Berg, A. Top-Down Fabrication of Sub-30 nm Monocrystalline Silicon Nanowires Using Conventional Microfabrication. *ACS Nano* **2009,** *3,* 3485–3492.

21. Chen, L. J. Silicon Nanowires: The Key Building Block for Future Electronic Devices. *J. Mater. Chem.* **2007,** *17,* 4639–4643.

22. Kelzenberg, M. D.; Turner-Evans, D. B.; Kayes, B. M.; Filler, M. A.; Putnam, M. C.; Lewis, N. S.; Atwater, H. A. Photovoltaic Measurements in Single-Nanowire Silicon Solar Cells. *Nano Lett.* **2008,** *8,* 710–714.

23. Yu, D. P.; Bai, Z. G.; Ding, Y.; Hang, Q. L.; Zhang, H. Z.; Wang, J. J.; Zou, Y. H.; Qian, W.; Xiong, G. C.; Zhou, H. T.; Feng, S. Q. Nanoscale Silicon Wires Synthesized Using Simple Physical Evaporation. *Appl. Phys. Lett.* **1998,** *72,* 3458–3460.

24. Ma, D. D. D.; Lee, C. S.; Au, F. C. K.; Tong, S. Y.; Lee, S. T. Small-Diameter Silicon Nanowire Surfaces. *Science* **2003,** *299,* 1874–1877.

25. Wang, N.; Tang, Y. H.; Zhang, Y. F.; Lee, C. S.; Lee, S. T. Nucleation and Growth of Si Nanowires from Silicon Oxide. *Phys. Rev. B* **1998,** *58,* R16024–R16026.

26. Teo, B. K.; Li, C. P; Sun, X. H.; Wong, N. B.; Lee, S. T. Silicon−Silica Nanowires, Nanotubes, and Biaxial Nanowires: Inside, Outside, and Side-by-Side Growth of Silicon *versus* Silica on Zeolite. *Inorg. Chem.* **2003,** *42,* 6723–6728.

27. Tu, Y; Tersoff, J. Structure and Energetics of the Si−SiO₂ Interface. *Phys. Rev. Lett.* **2000,** *84,* 4393–4396.

28. Tu, Y; Tersoff, J.; Grinstein, G.; Vanderbilt, D. Properties of a Continuous-Random-Network Model for Amorphous Systems. *Phys. Rev. Lett.* **1998,** *81,* 4899–4902.

29. Wooten, F.; Winer, K.; Weaire, D. Computer Generation of Structural Models of Amorphous Si and Ge. *Phys. Rev. Lett.* **1985,** *54,* 1392–1395.

30. Keating, P. N. Effect of Invariance Requirements on the Elastic Strain Energy of Crystals with Application to the Diamond Structure. *Phys. Rev.* **1966,** *145,* 637–645.

31. Ramos, L. E.; Furthmüller, J.; Bechstedt, F. Effect of Backbond Oxidation on Silicon Nanocrystallites. *Phys. Rev. B* **2004,** *70,* 033311.

32. Ramos, L. E.; Furthmüller, J.; Bechstedt, F. Influence of Oxygen on Optical Properties of Si Nanocrystallites. *Appl. Phys. Lett.* **2005,** *87,* 143113.

33. Fagas, G; Greer, J. C. Ballistic Conductance in Oxidized Si Nanowires. *Nano Lett.* **2009,** *9,* 1856–1860.

34. Liu, H. I.; Biegelsen, D. K.; Ponce, F. A.; Johnson, N. M.; Pease, R. F. W. Self-Limiting Oxidation for Fabricating Sub-5 nm Silicon Nanowires. *Appl. Phys. Lett.* **1994,** *64,* 1383–1385.

35. Hofmeister, H.; Huisken, F.; Kohn, B. Lattice Contraction in Nanosized Silicon Particles Produced by Laser Pyrolysis of Silane. *Eur. Phys. J. D* **1999,** *9,* 137–140.

36. Morales, A. M.; Lieber, C. M. A Laser Ablation Method for the Synthesis of Crystalline Semiconductor Nanowires. *Science* **1998,** *279,* 208–211.

37. Adolph, B.; Furthmüller, J.; Bechstedt, F. Optical Properties of Semiconductors Using Projector-Augmented Waves. *Phys. Rev. B* **2001,** *63,* 125108.

38. Bondi, R. J.; Lee, S.; Hwang, G. S. First-Principles Study of the Mechanical and Optical Properties of Amorphous Hydrogenated Silicon and Silicon-Rich Silicon Oxide. *Phys. Rev. B* **2010,** *81,* 195207.

39. Bondi, R. J.; Lee, S.; Hwang, G. S. Role of Structural Disorder in Optical Absorption in Silicon. *Phys. Rev. B* **2010,** *82,* 115214.

40. Bruneval, F.; Botti, S.; Reining, L. Comment on "Quantum Confinement and Electronic Properties of Silicon Nanowires". *Phys. Rev. Lett.* **2005,** *94,* 219701.

41. Sundari, S. T.; Raghavan, G. Measure of Disorder in Tetrahedrally Bonded Semiconductors. *Appl. Phys. Lett.* **2005,** *86,* 241906.

42. Yu, P. Y.; Cardona, M. *Fundamentals of Semiconductors*; Springer-Verlag: New York, 2001.

43. Levine, I. N. *Physical Chemistry*; McGraw-Hill: St. Louis, MO, 1995; pp 632−633.

44. Carrier, P.; Lewis, L. J.; Dharma-wardana, M. W. C. Optical Properties of Structurally Relaxed Si/SiO₂ Superlattices: The Role of Bonding at Interfaces. *Phys. Rev. B* **2002,** *65,* 165339.

45. Suk, S. D.; Li, M.; Yeoh, Y. Y.; Yeo, K. H.; Cho, K. H.; Ku, I. K.; Cho, H.; Jang, W.; Kim, D.-W.; Park, D.; *et al.* Investigation of Nanowire Size Dependency on TSNWFET. *IEEE Int. Electron Devices Meeting* **2007,** *1,* 891–894.

46. Pollak, F. H.; Shen, H. Photoreflectance Characterization of Semiconductors and Semiconductor Heterostructures. *J. Electron. Mater.* **1990,** *19,* 399–406.

47. Seraphin, B. O.; Bottka, N. Band-Structure Analysis from Electro-Reflectance Studies. *Phys. Rev.* **1966,** *145,* 628–636.

48. Cardona, M. *Modulation Spectroscopy*; Academic: New York, 1969.

49. Karazhanov, S. Zh.; Kroll, P.; Holt, A.; Bentzen, A.; Ulyashin, A. Comparative Analysis of Electronic Structure and Optical Properties of Crystalline and Amorphous Silicon Nitrides. *J. Appl. Phys.* **2009,** *106,* 053717.

50. Giri, P. K.; Tripurasundari, S.; Raghavan, G.; Panigrahi, B. K.; Magudapathy, P.; Nair, K. G. M.; Tyagi, A. K. Crystalline to Amorphous Transition and Band Structure Evolution in Ion-Damaged Silicon Studied by Spectroscopic Ellipsometry. *J. Appl. Phys.* **2001,** *90,* 659–669.

51. Mauri, F.; Pasquarello, A.; Pfrommer, B. G.; Yoon, Y.-G.; Louie, S. G. Si−O−Si Bond-Angle Distribution in Vitreous Silica from First-Principles ²⁹Si NMR Analysis. *Phys. Rev. B* **2000,** *62,* R4786–R4789.

52. Perdew, J. P.; Wang, Y. Accurate and Simple Analytic Representation of the Electron-Gas Correlation Energy. *Phys. Rev. B* **1992,** *45,* 13244.

53. Kresse, G.; Furthmüller, J. Efficient Iterative Schemes for *Ab-Initio* Total-Energy Calculations Using a Plane-Wave Basis Set. *Phys. Rev. B* **1996,** *54,* 11169–11186.

54. Kresse, G.; Furthmüller, J. *VASP the Guide*; Vienna University of Technology: Vienna, 2001.

55. Vanderbilt, D. Soft Self-Consistent Pseudopotentials in a Generalized Eigenvalue Formalism. *Phys. Rev. B* **1990,** *41,* 7892–7895.

56. Blöchl, P. E. Projector Augmented-Wave Method. *Phys. Rev. B* **1994,** *50,* 17953–17979.

57. Furthmüller, J. http://www.freeware.vasp.de/VASP/optics 2010.